Journal of Fluids and Structures (2001) **15,** 1061–1088
doi:10.1006/jfls.2001.0392, available online at http://www.idealibrary.com on IDEAL®

VISCOUS FLUTTER OF A FINITE ELASTIC MEMBRANE IN POISEUILLE FLOW

L. HUANG

Department of Mechanical Engineering, The Hong Kong Polytechnic University Kowloon, Hong Kong

(Received 1 June 2000, and in final form 8 June 2001)

Flow-induced vibration in a collapsible tube is relevant to many biomedical applications including the human respiratory system. This paper presents a linear analysis of the coupling between Poiseuille flow and a tensioned membrane of finite length using an eigenvalue approach. The undisturbed state of the channel flow is perfectly parallel. To some extent, this configuration bridges the gap between two types of theoretical models: one for the travelling-wave flutter in an infinite, flexible channel, and the other for the self-induced oscillation of a collapsing section of a Starling-resistor tube. In our study, we focus on the parameter range where the wall-to-fluid mass ratio is high (100), and the Reynolds number based on the maximum flow velocity in the channel is moderately high (200). Eigenmodes representing both static divergence and flutter are found. Particular attention is paid to the energetics of flutter modes. It is shown that energy transfer from the flow to the membrane occurs as a result of unstable, downstream-travelling waves, while the upstream-travelling waves are stable and release most of the transferred energy back to the flow. Coupling between different *in vacuo* modes offers another view of the origin of energy transfer. In addition, an energy conservation analysis similar to the one used in aeroacoustics is carried out. It is shown that terms directly proportional to fluid viscosity contribute most to the production of fluctuation energy, leading to a special type of dynamic instability which resembles both Tollmien–Schlichting instability in the sense that the fluid viscosity destabilises, and traditional travelling wave flutter since the structural damping plays the role of stabilising. Effects of the membrane mass, length and structural damping are also studied. The characteristics of the membrane flutter are found to depend crucially on the upstream and downstream boundary conditions.

1. INTRODUCTION

STUDIES OF FLOW THROUGH COLLAPSIBLE TUBES are relevant to many physiological phenomena of blood circulation and respiration. Virtually, all fluid-carrying vessels in the human body are elastic and collapsible (Caro *et al.* 1978), so are the bronchial airways (Grotberg 1994). Human snoring (Huang *et al.* 1995) and wheezing (Gavriely *et al.* 1989) are two examples of human airway oscillation. Although some effort is made in the present study to relate the controlling parameters to physiological phenomena, the main motivation is theoretical clarification of the flutter mechanism. The remainder of this section summarises three aspects of theoretical development in the studies of flow through collapsible tubes and two-dimensional flexible channels: (i) earlier potential flow models, (ii) the separated flow/vortex wave models, and (iii) travelling-wave flutter in infinite channels. Whilst most theories focus on a certain range of parameters, most notably the structure-to-fluid mass ratio, our summary is only concerned with the general conclusions instead of parametric variations. The summary is also restricted to two-dimensional channel configurations.

0889–9746/01/071061 + 28 $35.00/0

Earlier theoretical studies, e.g. by Shapiro (1977), began with a one-dimensional model of uniform flow in an elastic tube whose deformation was assumed to follow a tube-law relating the cross-sectional area with the transmural pressure (external minus internal). The tube law was a local function which did not contain any time variable. Matsuzaki & Fung (1977, 1979) considered two-dimensional models in which the flexible wall had a finite length, but the flow was again assumed to be a potential flow. Divergence was invariably predicted, and it was the only instability when structural damping was included. Wall oscillations were predicted by nonlinear "extrapolation" of the collapse and were sometimes referred to as "flutter". Models of this kind did capture the essence of flexible tube collapse. However, laboratory experiments and physiological evidence all suggested that a collapsing tube experienced oscillations of various types. Obviously, most structural oscillations started with small amplitudes which grew in time, and this required the transfer of energy from the flow to the structural vibration which presumably had to overcome certain structural damping. The search was on to find the mechanism for this energy transfer. Before we go on to describe the brief history of research in this area, it is necessary to clarify some terminology. In mechanics, we often refer to the event of tube collapse (or inflation) as a static instability or simply divergence. Similarly, we call oscillations that follow the collapse a dynamic instability or flutter. But the use of the word "flutter" has not been consistent in the literature. In our study, we choose to define flutter as a self-induced structural vibration caused by linear disturbances. Mathematically, flutter here is simply defined as an eigenmode with a finite frequency. It differs from the so-called post-divergence flutter (or flapping mode oscillation) as described by Weaver & Païdoussis (1977). The latter is a nonlinear manifestation of the tube collapse, i.e. a limit cycle oscillation. Some of these oscillations were also recently simulated by Luo & Pedley (1996, 1998) using a computational model quite similar to the one used in the present study. But it must be emphasized that the oscillations predicted in their studies have different features. They involve vortex shedding, which might be the driving force behind the instability at the late stage of a certainly nonlinear process. Flow-induced oscillations of this type are beyond the scope of our definition of linear flutter in a parallel flow, despite the fact that the two studies may contribute to the understanding of different aspects of essentially the same physiological phenomena.

We now describe experimental findings starting with the experiment of Weaver & Païdoussis (1977). Travelling waves were also observed downstream of the site of collapse, but they were believed to be initiated by divergence. The air flow was blown through a silicone rubber tube which was pre-flattened. The internal pressure was higher than the external pressure, contrasting with more typical experiments of collapsible-tube flow in which the external pressure was higher. The latter is commonly known as a Starling resistor, see e.g. Conrad (1969) and Bertram *et al.* (1990). In such a device, a segment of rubber tube is clamped at its up- and downstream ends and surrounded by a pressure chamber which controls the transmural pressure. Due to friction, the flow at the downstream end of the tube has the lowest pressure and, at a certain volume flow rate, the tube first buckles near the downstream clamp, forming a "neck". Further decrease in the downstream pressure accelerates the flow but narrows the neck, and a point is reached when the volume flow rate attains its peak value. Upon further increase in the driving pressure, oscillations of several distinct frequencies, as well as random vibrations, may follow. The experiments by Bertram and his colleagues were the most systematic, [e.g., Bertram *et al.* (1990), Bertram & Godbole (1997) and Bertram & Castles (1999)], and a brief review was given by Kamm & Pedley (1989). Most experiments were carried out using water as the fluid medium, but a few using air were also reported, e.g. by Gavriely *et al.* (1989) for wheezing, and in a simple rig by Huang *et al.* (1995) for pharyngeal snoring.

Presumably, the essence of some of these oscillation phenomena is nonlinear, and one of the main features is the unsteady flow separation and vortex shedding downstream of the oscillating wall constriction. Pedley and his colleagues have persistently pursued this line of modelling, which ranged from the vortex wave (Pedley & Stephanoff 1985), the lumped parameter modelling of the coupling of the flow separation and wall motion (Cancelli & Pedley 1985; Jensen 1990), to the more recent two-dimensional numerical simulation of the true mechanics of fluid–structure interactions (Luo & Pedley 1996, 1998). The latter dealt with large amplitude, self-excited oscillations, and demonstrated the phase difference between the wall displacement and wall pressure, a necessary ingredient for fluid-wall energy transfer. Similar simulations were also developed by Pedrizzetti (1998) and Tang *et al.* (1999) for slightly different configurations. With further development along this line, we can expect further insight into the physics of such energy transfer, and the efforts in this area may eventually merge with those in the area of vortex-shedding-induced vibration of cylinders and other cross-flow applications. However, the intricacy of the collapsible-tube flow has already attracted the attention of those studying the engineering problem of drag reduction and the delay of laminar flow transition (Davies & Carpenter 1997*b*). The results of these studies are briefly summarised below in the general framework of linear flutter with parallel flows.

In a quite separate line of pursuit, most notably by Grotberg and his colleagues, the search on the mechanism of fluid-wall energy transfer has been focused on the configuration of an infinitely long, parallel-sided channel whose undisturbed flow state is unidirectional. The mathematical appeal of a simple travelling-wave instability has certainly played a part in the development of such theoretical models. This model also has the potential to explain elegantly the phenomena of flow limitation in a way similar to the choking of compressible flow through a contraction–expansion nozzle. Attempts were made by LaRose & Grotberg (1997) to compare the results of a travelling-wave theory with oscillations measured in a Starling-resistor experiment. It is clear that a more satisfactory comparison must be made with a deliberate laboratory model in which the undisturbed state is free of unsteady flow separation. So far, there has been no serious attempt to create such a laboratory experiment, except, perhaps, that by Kececioglu *et al.* (1981) in which gravity was used to balance out the internal pressure gradient of water flow through the flexible tube. If similar measures are taken in a Starling resistor, one might be able to achieve a uniform transmural pressure along the tube. One of the first theoretical models for flutter came as an *ad hoc* Darcy friction term representing the effect of viscosity (Grotberg & Reiss 1984). Flutter was predicted and the approximate theory was later shown to be consistent with results from the full Orr–Sommerfeld system when fluid viscosity and structural damping were taken to zero simultaneously with the ratio of $\mathcal{O}(1)$ (Grotberg & Shee 1985). This model was recently upgraded by the solution for the full Orr–Sommerfeld system (LaRose & Grotberg 1997), and flutter was again predicted. The base flow chosen was a developing flow, a natural development of its predecessor which was a plug flow with Darcy-friction correction; but it is interesting to note that the physical intuition demonstrated in the Darcy friction model bears some resemblance to the physics shown in the present model which demonstrates that fluid viscosity plays an essential role in bringing about flutter of the finite-length membrane.

In a parallel development due to Davies & Carpenter (1997*b*), whose main motivation was to delay the laminar flow transition and reduce drag, the Orr–Sommerfeld equation was solved numerically for the Poiseuille flow to show what they called the travelling-wave flutter on the flexible channel walls. Modes in which the two walls moved in step (antisymmetrical in vibration velocity) were also considered and were found to be less critical than their symmetrical counterparts. Davies and Carpenter went further, to show that the Tollmien–Schlichting instability (TSI) could interact with the travelling-wave flutter, and that they might merge under certain conditions. However, it is generally agreed that TSI,

which behaves in a way opposite to the travelling-wave flutter with respect to the effect of structural damping, is not seen as relevant in the physiological context. The relevant features of TSI are: (a) TSI primarily occurs over rigid walls and in antisymmetric mode, and can be delayed by the wall compliance, and (b) TSI is destabilised by wall damping. For a more thorough discussion of TSI and its interaction with other instabilities, including travelling-wave flutter and Kelvin–Helmholtz instability, the reader is referred to the work of Carpenter & Garrad (1986) and a more recent work by Davies & Carpenter (1997*a*) in a geometric configuration quite similar to what we consider here. Again, it is interesting to note that the viscous flutter shown in the present model appears to differ from both TSI and travelling-wave flutter in the studies of Davies and Carpenter in terms of the role played by fluid viscosity and wall damping.

In yet another parallel development, due to the present author (Huang 1998), a Poiseuille flow model was also adopted, but attention was focused on the inviscid shear flow effect for which the Orr–Sommerfeld equation was reduced to the Rayleigh equation. Flutter was also found, together with a special phenomenon of the reversal of the collapsing tendency associated with the Bernoulli effect for potential flows. Note that the Bernoulli effect dominates the mechanics of all earlier models which predict only static divergence in the linear framework. Dealing with a much simpler mathematical model, we were able to present a more complete picture of the physics involved. The mechanism of the fluid-wall energy transfer was identified with Miles' (1957) theory of water wave generation by shearing wind with vorticity gradient, and the reversal of the Bernoulli effect was found to be a channel-wall amplification of the Miles mechanism. It was also shown that the pressure developed a component in phase with the wave slope when the surface wave was slower than the maximum flow speed in the shear flow profile. This condition is related to the existence of the so-called critical layer and was shown by Lord Kelvin to induce a "cat's-eye" vortex pattern when viewed from the travelling surface wave. Our conclusion that the flutter mechanism was essentially a shear flow phenomenon was in perfect agreement with the full Orr–Sommerfeld solution of Davies & Carpenter (1997*b*), who went on to state that even TSI behaved as an inviscid instability when it interacted and merged with the travelling-wave flutter.

Part of the motivation for the current study is to test the following conjecture. If Miles' mechanism of wave drag, hence fluid-wall energy transfer, is robust, flutter should also occur on a finite membrane which experiences travelling surface waves in both directions. In contrast to the conclusions reached in the inviscid flow model, it turns out that the similar shear-flow terms are overshadowed by the viscous terms in the current model of viscous flow over a finite-length membrane, and the viscous flutter mechanism is more closely related to the velocity gradient instead of the vorticity gradient as was the case for the shear-flow flutter. In what follows, the linearized Navier–Stokes equations are solved numerically, and it is found that flutter exists alongside divergence. The nature of the numerical calculation leads us to consider a model of finite length for the duct upstream and downstream of the membrane. Two typical sets of boundary conditions are used, and they simulate, respectively, blowing and suction flows through a finite channel with an elastic insertion. It is shown that the changes of these boundary conditions have drastic effects on the transient flow characteristics, leading to a totally different form of eigenvibration.

2. THEORY

2.1. Theoretical Model

We consider a two-dimensional channel of height h^*, through which a fluid of density ρ^* flows with a Poiseuille velocity distribution with maximum velocity at the centre, $U^*_{\max}$.

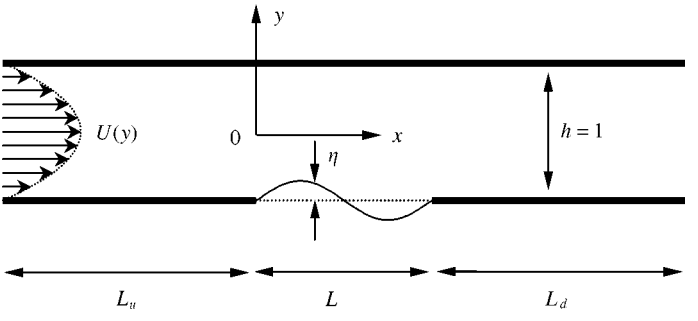

Figure 1. The model configuration.

Here $h^*, \rho^*, U^*_{\max}$ are chosen as the length, density and velocity scales for normalisation. The time scale is $h^*/U^*_{\max}$ and the pressure or stress scale is $\rho^* U^{*2}_{\max}$. Symbols without asterisks denote dimensionless variables. So, the dimensionless height is $h = 1$, and the dimensionless velocity distribution is $U(y) = 1 - 4y^2$. As shown in Figure 1 with dimensionless labels, the upper rigid wall lies at $y = 0{\cdot}5$, while the lower wall incorporating the elastic membrane is located at $y = -0{\cdot}5$. The membrane has a length of L, and is subject to tensile stress. Bending stiffness and elastic support could also be included, but it is felt that the underlying physics is partly shared by that of the tensile force. However, in the long-wave limit, the effect of an elastic foundation differs from that of tensile and bending forces. It would be interesting to investigate the relationship between this model and some traditional tube-law models, but this is excluded in the present studies partly because of the large number of controlling parameters. As a result, long-wave static divergence instability does not appear in the current model. The upstream and downstream length of the channel are L_u and L_d, respectively. The velocity profile at the channel entrance is assumed to be fully developed, and the use of L_u and L_d is solely associated with the specification of boundary conditions for the flow perturbation. When there is no perturbation, steady Poiseuille flow inside the tube creates a pressure gradient which tends to collapse the membrane if the external pressure is a constant. For simplicity, we assume an external pressure distribution identical to the internal pressure associated with the steady flow. Such an external pressure distribution is unrealistic, but the assumption is purposefully made to examine whether a nominally flat membrane can also experience flutter in a way a buckled tube does. The task now is to find the critical flow speed for the membrane to begin to collapse or experience flow-induced oscillation, and the characteristics of any such eigenvibrations.

The linear dynamics of the tensioned membrane is governed by

$$m\frac{\partial^2\eta}{\partial t^2} + D\frac{\partial\eta}{\partial t} - T\frac{\partial^2\eta}{\partial x^2} + p_1 = 0, \tag{1}$$

where η is the membrane displacement, m, D and T are the dimensionless membrane mass per unit length, damping coefficient, and the uniform tension, defined as follows:

$$m = \frac{m^*}{\rho^* h^*}, \quad D = \frac{D^*}{\rho^* U^*_{\max}}, \quad T = \frac{T^*}{\rho^* U^{*2}_{\max} h^*}, \tag{2}$$

while p_1 is the normalised fluid normal stress which will be related to the membrane displacement η through the fluid-dynamics model. Note that, in general, D is a function of

vibration frequency, whose dimensionless version ω is defined as

$$\omega = \omega^* h^* / U^*_{\max}, \tag{3}$$

as well as many other properties in a tensioned membrane. The issue of damping on a tensioned membrane is a complicated one (Berry 1992). Nevertheless, the simple concept of a constant loss factor σ will be adopted here; σ is the ratio of energy damping per radian to the maximum potential energy, and is related to D by the following expression:

$$\sigma = D/m\omega.$$

The damping term, $D(\partial\eta/\partial t)$, in equation (1) will be absorbed into the inertia term to form a complex inertia term, $m(1 - \mathrm{i}\sigma)\partial^2\eta/\partial t^2$, for harmonic vibrations of time dependency $\mathrm{e}^{\mathrm{i}\omega t}$; σ will be referred to as either a loss factor, or simply damping in a later discussion. Equation (1) will then be solved by the standard Galerkin method to find the eigen frequency, ω.

For the fluid part, incompressible flow is assumed, and the Navier–Stokes equation is

$$\frac{D}{Dt}\mathbf{V} + \nabla p = \mu\nabla^2\mathbf{V}, \quad \mu = \frac{\mu^*}{\rho^* U^*_{\max} h^*}, \tag{4}$$

where $\mathbf{V}$ is the full flow velocity (normalised by $U^*_{\max}$) and p is the full pressure (normalised by $\rho^* U^{*2}_{\max}$), μ is the dimensionless fluid viscosity, or the inverse of Reynolds number based on $U^*_{\max}$ and the channel height h^*. This equation is linearised by the following expressions:

$$\mathbf{V} = \{U(y) + u, v\}, \quad p = p_0(x) + p',$$

where u, v are the components of flow perturbation velocity in the x and y directions, respectively, and $p_0(x)$ is the pressure gradient created by the viscous friction of the steady flow,

$$\partial p_0/\partial x = \mu U''(y).$$

p' is the pressure perturbation, but the fluid loading on the membrane is the total normal stress denoted as p_1,

$$p_1 = \left[p' - 2\mu \frac{\partial v}{\partial y} \right]_{\text{membrane}}, \tag{5}$$

to be evaluated on the membrane surface. The final linear set of equations, including the mass conservation equation, become

$$\begin{aligned} \frac{\partial u}{\partial t} + U\frac{\partial u}{\partial x} + v\frac{\mathrm{d}U}{\mathrm{d}y} + \frac{\partial p'}{\partial x} - \mu\nabla^2 u = 0, \\ \frac{\partial v}{\partial t} + U\frac{\partial v}{\partial x} + \frac{\partial p'}{\partial y} - \mu\nabla^2 v = 0, \\ \frac{\partial u}{\partial x} + \frac{\partial v}{\partial y} = 0. \end{aligned} \tag{6}$$

The three linear perturbation quantities, u, v and p', vanish when there is no wall vibration. The time derivative, $\partial/\partial t$, is replaced by $\mathrm{i}\omega$ in a harmonic oscillation problem. The no-slip condition, $u = v = 0$, is imposed on all rigid walls. At the inlet, $x = -L_u$, the volume flow rate is fixed, hence zero perturbation, $u = 0$. It will be shown later that L_u has little effect on the results when this boundary condition is imposed. This condition is used together with $v = 0$ in viscous flow where most perturbations on v are expected to decay to

a minimal level at the upstream station. At the downstream, $p' = 0$ is specified to simulate an open end to the atmosphere. In fact, in situations like inspiratory flow into the lungs, constant downstream flow drafting, $u = v = 0$, is more appropriate, while the upstream pressure remains relatively constant, $p' = 0$. If the former is designated as a "blowing" flow condition, the latter may be called the "suction" flow condition. The effect of the change of up- and downstream boundary conditions is discussed later. On the membrane surface, where the mean flow vanishes, $U = 0$, the no-slip condition should also be imposed, which means

$$v_{y=-0{\cdot}5+\eta} \approx v_{y=-0{\cdot}5} = \frac{\partial \eta}{\partial t} = \mathrm{i}\omega\eta, \quad (u+U)_{y=-0{\cdot}5+\eta} = u_{y=-0{\cdot}5} + \eta U'(-0{\cdot}5) = 0.$$

Note that, on the nominal wall position, $y = -0{\cdot}5$, the axial velocity perturbation u does not vanish. The linear computation is then conducted in a rectangular domain without the complication of moving boundaries required in nonlinear calculations.

Strictly speaking, the membrane tension varies axially due to the viscous shear stress acting on the membrane. The ratio of the total shear stress acting on the membrane to the tension applied is found to be

$$\frac{\mu^*[\partial U^*/\partial y^*]_{y^*=-h^*/2} L^*}{T^*} = 4\mu L/T.$$

As long as this ratio is low, the axial variation of membrane tension can be ignored. As will be shown later, $4\mu L/T$ has the value of 0·22 when flutter is predicted for the "default" set of parameters used in the present paper (see Section 3.1). The ratio can be higher or lower when the controlling parameters vary. Nevertheless, the effect of the axial tension variation is not included in the present study, partly because of the large number of controlling parameters.

2.2. Method of Solution

The standard Galerkin approach is followed to solve the eigenvalue problem. The membrane displacement is decomposed into *in vacuo* modes:

$$\eta = \mathrm{e}^{\mathrm{i}\omega t} \sum_{n=1}^{\infty} A_n \sin(n\pi x/L), \tag{7}$$

where A_n is the modal amplitude. The fluid loading is related to these modal amplitudes by calculating the loading caused by individual modal vibration of unit amplitude,

$$p_1 = \sum_{n=1}^{\infty} p_1|_{\mathrm{mode}\,n} A_n,$$

in which the subscript "mode n" denotes the nth mode vibration of unit amplitude. The complete fluid loading is also sine-transformed to form a modal coefficient matrix of fluid loading, $\{P_{jn}\}$, in which the element P_{jn} represents the jth modal coefficient of fluid loading generated by the vibration of the nth *in vacuo* mode of unit amplitude, and is calculated by

$$P_{jn} = \frac{2}{L} \int_0^L p_1|_{\mathrm{mode}\,n} \sin(j\pi x/L)\,\mathrm{d}x. \tag{8}$$

The finite-element software package FEMLAB®, which is the extended version of the Partial Differential Equation Toolbox of the popular computing language MATLAB®, is used to solve the linearised Navier–Stokes problem. The technique of streamwise diffusion

is required to stabilise the solution, despite the fact that the two momentum equations come with viscosity. The error caused by the application of the artificial viscosity tends to zero when the mesh size vanishes. Numerical tests on energy conservation and other relationships (to be discussed later) show that a mesh size smaller than about 0·0025 near boundaries and 0·05 at the channel centre gives satisfactory results.

Combining equations (1), (7) and (8), we get

$$\begin{gathered} \Pi_j A_j + \sum_n P_{jn} A_n = 0, \quad j = 1, 2, 3, \cdots, N, \\ \Pi_j = m\omega^2(-1 + i\sigma) + T(j\pi/L)^2, \end{gathered} \tag{9}$$

where summation of j is not applied on the first term of the equation, $\Pi_j A_j$, N is the order of modal truncation. It will be shown later that $N = 10$ suffices for the range of parameters considered in the present study. The eigenequation becomes

$$Q = \det(\{P\} + \mathrm{diag}\{\Pi\}) = 0, \tag{10}$$

where $\{P\}$ means the modal coefficient matrix of fluid loading whose element is defined by equation (8), $\mathrm{diag}\{\Pi\}$ means the diagonal matrix formed by the vector with the structural property Π_j defined in equation (9).

The eigenvibration amplitudes A_j can be found once the eigenfrequency ω is known. The key issue now is the fluid loading matrix $\{P\}$ which is a function of three geometrical parameters (L_u, L_d, L), two membrane property parameters (m, σ), and two other controlling parameters (μ, T). The fluid viscosity μ is essentially the inverse of the Reynolds number, and it is more intuitive to refer to this controlling parameter as the flow speed. Assuming that we know the first five parameters, the stability problem is posed as follows. For a given tension T, find the minimum flow speed so that the eigenvibration is neutrally stable, namely when the eigenfrequency ω is purely real. Since Q in the eigenequation (10) is a highly nonlinear function of two variables, ω and μ, a reliable solution method would be a two-dimensional scan over a vast region of the two-variable space (ω, μ). Contour curves of $\mathscr{R}e[Q(\omega, \mu)] = 0$ and $\mathscr{I}m[Q(\omega, \mu)] = 0$ can be found by the MATLAB® code "contourc". The interception points of the two sets of contour curves are the solutions to the eigenequation $Q = 0$, and the eigensolution with the lowest flow speed (or highest μ) is identified as the critical speed beyond which instability occurs. However, this process involves too many calls to the FEMLAB® routine to find the fluid loading matrix $\{P\}$. An alternative procedure is introduced whereby the flow speed is fixed via specifying μ, but the membrane tension T varies. In this case, the number of calls to the FEMLAB® routine is determined by the number of scans over one independent variable, ω, as the fluid loading caused by the vibration of specified *in vacuo* modes is independent of the tensile force on the membrane. Eigenequation (10) is solved by the contour-crossing method over the alternative two-variable space of (ω, T), so that

$$\mathrm{Re}[Q(\omega, T)] = 0, \quad \mathrm{Im}[Q(\omega, T)] = 0. \tag{11}$$

Since T is tension normalised by $\rho^* U^{*2}_{\max} h^*$, a low flow velocity means a high value of T. If multiple solutions are found, the one with the highest value of T becomes the critical condition for membrane instability. The value of T for this condition is called the critical tension. If the eigenfrequency vanishes, the membrane experiences a static divergence; otherwise the eigenmode is associated with flutter.

At the eigensolution points, there are $N - 1$ independent equations in the set of N linear equations in (10), where N is the total number of *in vacuo* modes used. These are solved for the eigenvectors which are then normalised by the first mode amplitude A_1. The characteristic membrane displacement curve η is constructed from these complex amplitudes

according to equation (7). The fluid loading for the eigenvibrations can also be constructed by the linear superposition of the loadings calculated for different modes at the eigenfrequency.

The eigenvibration displacement $\eta(x,t)$ has to satisfy the boundary conditions of the pinned membrane at $x = 0, L$, and is therefore a standing wave. It can be decomposed into downstream- and upstream-travelling waves, which may be called, respectively, the incident and reflected waves denoted by subscripts i and r. Hence,

$$\begin{aligned} \sin(j\pi x/L) &= \frac{\mathrm{i}}{2}(\mathrm{e}^{-\mathrm{i}j\pi x/L} - \mathrm{e}^{+\mathrm{i}j\pi x/L}), \quad \eta = (\eta_i + \eta_r)\,\mathrm{e}^{\mathrm{i}\omega t}, \\ \eta_i &= \frac{\mathrm{i}}{2}\sum_j A_j \mathrm{e}^{-\mathrm{i}j\pi x/L}, \quad \eta_r = \frac{-\mathrm{i}}{2}\sum_j A_j \mathrm{e}^{+\mathrm{i}j\pi x/L}. \end{aligned} \tag{12}$$

The amplitude and phase angle distributions of incident (η_i) and reflected (η_r) waves are studied separately, so are the coupling between the total fluid loading with the decomposed elastic waves.

2.3. Energy Conservation

As we place much emphasis on the role of each physical ingredient in the process of energy transfer from the fluid flow to the vibration of the wall, and from the mean flow to fluctuations, some form of energy conservation analysis is very useful. To do so, we first review the practice in aeroacoustics where the perturbation energy density and its flux are defined, respectively, as

$$E^* = \frac{p^{*\prime 2}}{2\rho^* c^{*2}} + \frac{p^{*\prime}}{c^{*2}}(\mathbf{V}^* \cdot \mathbf{v}^*) + \frac{1}{2}\rho^*(|\mathbf{v}^*|^2), \quad \mathbf{I}^* = \left(\frac{p^{*\prime}}{\rho^*} + \mathbf{V}^* \cdot \mathbf{v}^*\right)(\rho^* \mathbf{v}^* + \rho^{*\prime}\mathbf{V}^*),$$

where c^* is the speed of sound, ρ^*, $\rho^{*\prime}$ are the fluid density and its perturbation, respectively, and $\mathbf{V}^*$, $\mathbf{v}^*$ are the mean flow and perturbation velocity, respectively. A conservation law of the form

$$\frac{\partial E^*}{\partial t^*} + \nabla^* \cdot \mathbf{I}^* = 0,$$

is established for sound propagation through inviscid, potential flows. The right-hand side does not vanish in other situations, and they can be called the sources of sound energy thus defined. It must be pointed out, however, that the second-order terms like these can only be loosely interpreted as energy density and energy fluxes, and they are in general not identical to the difference of energy in a perturbed state minus that of the undisturbed. This issue has been discussed at length in the study of sources of sound in the presence of flow, especially turbulent and inhomogeneous flow (Morfey 1971; Möhring 1971). There are two exceptions, however, where unambiguous physical interpretations are possible. One is classical acoustics where there is no mean flow, and the other, which is less well known, is sound propagation through potential flow. The flux ($\mathbf{I}^*$) thus defined is normally referred to as the Blokhintsev flux (Möhring 1971), which has a clear physical interpretation and is directly related to the energy transfer between fluid and structure. This is the main reason why we adopt this set of definitions. More precisely, the flux through a vibrating boundary corresponds to the energy transfer between sound and structure through the action of pressure perturbation $p^{*\prime}$. (The mathematical details for the more general case of viscous flow are presented below.) Applying this concept to a geometric configuration like Figure 1, with Poiseuille flow substituted by a potential flow, the integration of $\nabla^* \cdot \mathbf{I}^*$ over the rectangular domain occupied by the fluid is equal to the sum of fluxes through all

boundaries. Since $\mathbf{I}^*$ vanishes on all rigid walls, the fluid-to-membrane energy transfer can be calculated by adding together the sound energy flux coming into the calculation domain through the upstream and downstream boundaries. Knowing that there should not be any perturbation wave coming into the domain from the far field in either direction, which is the so-called causality condition, one immediately concludes that the membrane cannot absorb energy from flow, hence no flutter in a potential flow.

In the case of viscous flow, the situation is different. However, a similar conservation law can be derived for the configuration shown in Figure 1 by taking into account the viscosity effect and, for simplicity, excluding the compressibility effect ($\rho^{*\prime} = 0, c^* \to \infty$). We therefore define

$$E^* = \frac{1}{2}\rho^*(u^{*2} + v^{*2}), \quad \mathbf{I}^* = \rho^*\{u^*, v^*\}\left[\frac{p^{*\prime}}{\rho^*} + U^*u^*\right].$$

After normalising E^* by $\rho^* U_{\max}^{*2}$ and $\mathbf{I}^*$ by $\rho^* U_{\max}^{*3}$, the dimensionless form of energy conservation is written as

$$\frac{\partial E}{\partial t} + \nabla\cdot\mathbf{I} = S, \quad E = \frac{1}{2}(u^2 + v^2), \quad \mathbf{I} = (p' + Uu)\{u, v\}, \tag{13}$$

where S is the source of fluctuation energy to be found by substituting $\partial p'/\partial x$ and $\partial p'/\partial y$ in $\nabla\cdot\mathbf{I}$ with the pressure gradient given in the linearised momentum equations in equation (6). After some manipulation, the source terms are found as follows:

$$S = \underbrace{\nabla\cdot\nabla\mu\left(\frac{u^2 + v^2}{2}\right)}_{\mathbf{J}} \underbrace{- \mu(|\nabla u|^2 + |\nabla v|^2)}_{\Psi} \underbrace{- Uv\left(\frac{\partial v}{\partial x} - \frac{\partial u}{\partial y}\right)}_{\Theta}. \tag{14}$$

The three labelled groupings are given the names of viscous surface flux $\mathbf{J}$, viscous bulk damping Ψ, and vortical absorption Θ, respectively. All these terms vanish in inviscid potential flow. It might be tempting to group $\mathbf{J}$ with $\mathbf{I}$ and call $(\mathbf{I} - \mathbf{J})$ the new flux, but such a definition risks creating conceptual inconsistency as the energy density term E does not and cannot contain any term of viscous origin. Besides, as will be shown later, the value of the viscous surface source is found to be positive, at least in our studies; it is therefore convenient to interpret this term as a source. On the contrary, the value of the new flux $(I_n - J_n)$ is negative, which is somewhat against established physical intuition.

The energy flux from fluid to the membrane across the interface, where $U = 0$ and $v = \partial\eta/\partial t$, is $I_n = -p'v$, where $\mathbf{n}$ is the outward normal vector in $-y$ direction. Notice that pressure is not the only force acting on the membrane. The energy balance for the harmonic vibration of the membrane is found by multiplying equation (1) by the conjugate of vibration velocity $(\dot\eta)^*$, and integrating it over the membrane length,

$$\int_0^L [-m(1 - \mathrm{i}\sigma)\omega^2\eta(\dot\eta)^* - T\eta_{xx}(\dot\eta)^* + p_1(\dot\eta)^*]\,\mathrm{d}x = 0,$$

from which half of the real part yields the time-average energy balance:

$$\underbrace{\frac{1}{2}\mathscr{R}e\left[\int_0^L \sigma\omega|\dot\eta|^2\,\mathrm{d}x\right]}_{W_\sigma} = \underbrace{\frac{1}{2}\mathscr{R}e\left[\int_0^L(-p')(\dot\eta)^*\,\mathrm{d}x\right]}_{W_p} + \underbrace{\frac{1}{2}\mathscr{R}e\left[\int_0^L 2\mu\frac{\partial v}{\partial y}(\dot\eta)^*\,\mathrm{d}x\right]}_{W_\mu}. \tag{15}$$

Note that the asterisks outside the brackets denote conjugate instead of dimensional values. It is perhaps necessary to explain why the time-average of the term $\int_0^L T\eta_{xx}\dot{\eta}\,\mathrm{d}x$ is zero. Expanding $\eta_{xx}\dot{\eta}$ as

$$\eta_{xx}\dot{\eta} = \frac{\partial}{\partial x}(\eta_x\dot{\eta}) - \eta_x\frac{\partial}{\partial x}\dot{\eta} = \frac{\partial}{\partial x}(\eta_x\dot{\eta}) - \frac{1}{2}\frac{\partial}{\partial t}(\eta_x)^2,$$

we see that the first term on the right-hand side does not make any contribution to integration since the membrane is fixed ($\dot{\eta} = 0$) at both ends, nor does the second term for a stationary oscillation. As it turns out in our study of flutter modes, the viscous contribution, W_μ, is always negative, or stabilising, as might have been anticipated from the nature of the viscous diffusion of vertical momentum from the membrane surface, $\partial v/\partial y < 0$ for $v > 0$. Therefore, the behaviour of the energy flux term, W_p becomes crucial for the investigation of the origin of flutter mechanism.

Integrating equation (13) over the computational domain for the harmonic vibrations,

$$\underbrace{\int_0^1 I_n|_{\text{upstream}}\,\mathrm{d}y}_{F_u} + \underbrace{\int_0^1 I_n|_{\text{downstream}}\,\mathrm{d}y}_{F_d} + \underbrace{\int_0^L (-p')v\,\mathrm{d}x}_{F_m = W_p} = \underbrace{\oint J_n\,\mathrm{d}l}_{S_J} - \underbrace{\iint \Psi\,\mathrm{d}s}_{S_\Psi} - \underbrace{\iint \Theta\,\mathrm{d}s}_{S_\Theta}, \tag{16}$$

where the conjugation and time-average operations are omitted for brevity, I_n, J_n are the outward-going fluxes, $\mathrm{d}s$ is the elemental area and $\mathrm{d}l$ the elemental boundary length. The source integrals are denoted by S with subscripts indicating the source terms defined in equation (14), and fluxes are denoted by F with subscripts indicating the boundaries. The flux through the membrane, F_m, is equivalent to the part of work done on the membrane by normal pressure, W_p defined in equation (15). Combining equations (15) and (16), we get

$$W_p = S_J - S_\Psi - S_\Theta - F_u - F_d. \tag{17}$$

We can now trace the sources of fluid-to-structure energy transfer to the viscous surface source, S_J, viscous bulk damping, S_Ψ, and the vortical absorption S_Θ, while the energy radiation to the far field, $F_u, F_d \geq 0$, shares part of the fluctuation energy. As will be shown later, $S_J > 0$, and it dominates over the viscous damping S_Ψ, leading to a net positive contribution from the terms proportional to fluid viscosity, $S_J - S_\Psi > 0$. The aggregate effect of the fluid viscosity terms is found to be destabilising as in the case of Tollmien–Schilitchting waves, but the work done by the viscous normal stress, W_μ defined in equation (15), is stabilising. It will also be shown later that the two effects from fluid viscosity are found to compete with each other in the flutter eigenmode.

2.4. Elementary Modal Analysis

In order to appreciate the physics at the elementary level, the behaviour of the fluid flow driven by a specified modal vibration of the wall is analysed in detail. For mode 1 under the blowing-type of boundary conditions, the solution is shown in Figure 2. The basic parameters used are $L = 1{\cdot}5$, $L_u = L_d = 2$, $\mu = 1/200$, which will also serve as the default setting for the basic example in the next section. The driving frequency is $\omega = 0{\cdot}13$. Around 50 000 elements are used in the calculation and the relative error tolerance is 10^{-5}.

Figure 2(a) shows the real part of the perturbation velocity vector, $\{u, v\}$. The real part represents the actual situation at time $t = 0$ for a membrane harmonic vibration specified as $\eta = \sin(\pi x/L)\mathrm{e}^{\mathrm{i}\omega t}$. The membrane vibration velocity is $\dot{\eta} = \mathrm{i}\omega\sin(\pi x/L)$ and is illustrated by

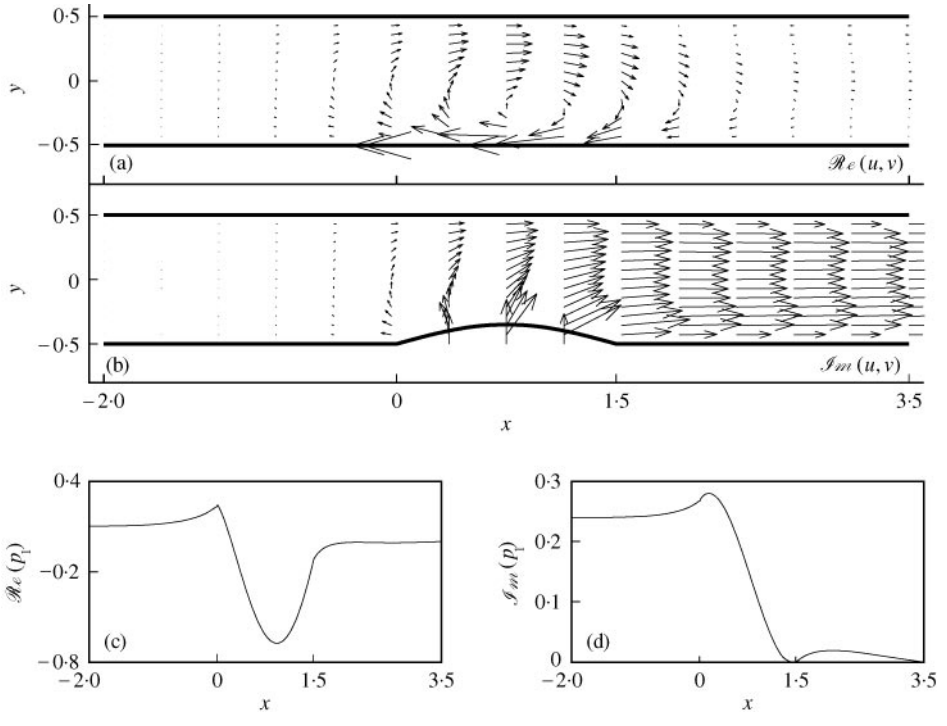

Figure 2. FEMLAB® solution of the linearised Navier–Stokes equations when the membrane undergoes a specified first mode vibration with $\omega = 0{\cdot}13$. (a) and (b) show, respectively, the real and imaginary parts of the perturbation velocity vectors, with the wall positions illustrated by the thick solid lines; (c) and (d) show, respectively, the real and imaginary parts of the fluid loading on the membrane. Note that the vibration velocity is purely imaginary in terms of phase angle.

the hump in Figure 2(b), $\mathscr{R}e(\dot{\eta})$ being zero for Figure 2(a). The pattern of $\mathscr{R}e(u,v)$ is essentially a clockwise "vortex" on the leeward side of the displaced membrane. Strictly speaking, streamlines constructed by the total velocity $\{U+u, v\}$ continue to be as in parallel flow since the linear perturbation is infinitesimal. However, the analysis of the perturbation velocity patterns in terms of real and imaginary parts will help our understanding of the details of each physical ingredient in the fluid–structure interaction. The pattern can be interpreted as follows. The fluid particles near the wall carry more vorticity than those near the centre, and the upward wall displacement creates a local excess clockwise vorticity. The excess vorticity is highest at $y = -0{\cdot}5$, but the convection effect of this vorticity, $U(\partial v/\partial x - \partial u/\partial y)$, is concentrated somewhere away from the membrane, and coincides well with the above-mentioned perturbation "vortex" pattern. The detailed explanation of why a perturbation "vortex" is anchored on the leeward side of the membrane can be found in Huang (1998). As the perturbation vorticity is convected by the mean flow, it is subject to an upward force which some call the "vortex force" (Lighthill 1962). Mathematically, this force is balanced out by a positive vertical pressure gradient, as is shown by the linearised vertical momentum equation for the inviscid, steady flow, $\partial p'/\partial y = -\partial v/\partial x$, in which $\partial v/\partial x < 0$ for the clockwise perturbation vorticity. As a result, the leeward side of the membrane wall experiences the lowest pressure. This can be seen from Figure 2(c), which gives the real part of the normal stress, $\mathscr{R}e(p_1)$, in-phase with the displacement η. Overall, $\mathscr{R}e(p_1)$ is negative over the membrane region, $x \in [0, L]$, which indicates a tendency for the membrane to collapse. This effect is shared by the passage

TABLE 1
Results of energy conservation analysis for mode 1

Source term	Result	Output flux	Result
Viscous source	$S_J = 0{\cdot}2390$	To upstream	$F_u = 0$
Bulk dissipation	$S_\Psi = 0{\cdot}2126$	To downstream	$F_d = 0{\cdot}0076$
Vortical absorption	$S_\Theta = 0{\cdot}0284$	To membrane	$F_m = -0{\cdot}0094$
Net source	-0.0019	Net flux	$-0{\cdot}0017$

narrowing of a uniform flow, namely the Bernoulli effect. However, an asymmetric pattern of $\mathscr{R}e(p_1)$ with respect to the membrane centre, $x = L/2$, is created by the shear flow. The positive value of $\mathscr{R}e(p_1)$ over part of the upstream half of the membrane indicates a reversal of the Bernoulli effect (Huang 1998).

Figure 2(b) shows the imaginary part of the velocity perturbation, which is inphase with the membrane vibration velocity whose distribution is shown as a hump on the lower wall. The volume of fluid displaced by the membrane is drained through the downstream boundary since the upstream end has a boundary condition of zero velocity perturbation. Figure 2(d) is the imaginary part of p_1, or $\mathscr{I}m(p_1)$, which is inphase with the membrane vibration velocity. A positive value indicates that the membrane has to do work against the flow and is therefore not prone to vibration. It is shown later that, when the membrane loses stability, the actual eigenvibration is far from being the first *in vacuo* mode shown in Figure 2.

The energy conservation analysis is shown in Table 1. The first column gives the results of source term integration, where the sources are specified in equation (14). The second column shows the integrated fluxes across three borders, in which the one through the membrane accounts for the work done by the pressure term alone, $W_p = F_m$; $W_p < 0$ means that the membrane does work on the fluid when it undergoes a *specified* mode 1 vibration. Ideally, the net source should be equal to the net flux going out. The numerical error is 0·0002, which is 2% of F_m, or 0·08% of the largest term S_J in the energy conservation equations (13) and (14). If one combines the two viscous terms together, the total viscous source is $S_J - S_\Psi = 0{\cdot}0264$, which is comparable in magnitude to the energy absorbed by the vorticity perturbation, S_Θ. To a certain extent, the results come as a surprise, since the viscous terms contribute to the production of fluctuation energy, while the perturbation of vorticity field absorbs it, which is opposite to the effect of vorticity gradient shown for the inviscid shear flow in Huang (1998). The vortical absorption can be further analysed by decomposing the term $Uv(\partial v/\partial x - \partial u/\partial y)$ into the coupling of real parts and imaginary parts of vertical velocity v and vorticity $(\partial v/\partial x - \partial u/\partial y)$, which works out as 0·0289 and $-0{\cdot}0005$. Therefore, the real part dominates and it apparently does so by the convection of a perturbation "vortex" shown in Figure 2(a). The vorticity $(\partial v/\partial x - \partial u/\partial y) < 0$, or clockwise, but the vertical velocity is upwards in the upstream part but downwards in the downstream part. The up-drafting of clockwise vorticity produces fluctuation energy, while down-drafting of clockwise vorticity further downstream absorbs it. The total is absorption in this case, indicating a general trend of more down-drafting action downstream of the narrowest point in the flow passage.

By far the most dominant source term is the viscous surface source S_J. The outward going flux of **J** is calculated as follows on the membrane surface, where the source term is significant,

$$J_n = -\mu(u\partial u/\partial y + v\partial v/\partial y).$$

We find numerically that $J_n > 0$ and $|u\partial u/\partial y| \gg |v\partial v/\partial y|$, and that J_n does not change sign as $\mu \to 0$. The first term in J_n is dominant and is analysed in more detail. On the boundary of $y = -0{\cdot}5$, the axial velocity is $u = -\eta(\mathrm{d}U/\mathrm{d}y) < 0$. But this perturbation decays away from the wall, so that $\partial u/\partial y > 0$, hence $-\mu u\partial u/\partial y > 0$. This term can be interpreted as the power provided by some external force causing the fluid to "slip" to the left on the geometrical border of $y = -0{\cdot}5$. In essence, the energy transfer from the mean flow to fluctuation finds its way through the no-slip boundary condition which requires $u = -\eta(\mathrm{d}U/\mathrm{d}y)$ on the geometric interface $y = -0{\cdot}5$. This mechanism is similar to the interface coupling investigated by Kumaran (1995*a*, *b*), who treated the problem of Stokes flow instability over a viscoelastic gel where the fluid–gel interface has a strain discontinuity similar to $\mathrm{d}U/\mathrm{d}y$ in our model.

3. RESULTS

The system has six control parameters, and the following values are chosen as the "default" setting for the basic example and parametric studies:

$$L_u = 2, \quad L = 1{\cdot}5, \quad L_d = 2, \quad \mu = 1/200, \quad m = 100, \quad \sigma = 0{\cdot}5\%. \tag{18}$$

Incidentally, the mass ratio and the flow Reynolds number used here are approximately those found in the respiratory flow in the 8th generation of the bronchial structure of human lungs (Fung 1993). The upstream and downstream distances, L_u, L_d, are, however, chosen purely for the computational convenience. They are shorter than those needed in a nonlinear calculation, where the solution has to be stable for the steady flow with flow separation (Luo & Pedley 1996). The baseline flow used in the present study is an attached flow, and there is no need to specify a long downstream distance in order to stabilise the computational scheme. In fact, the upstream and downstream distances control the resistance and inertia for the linear perturbation, and their effects on the eigenvalues are studied later. It is found that the upstream distance, L_u, has little effect on results when $u = v = 0$ is specified at the upstream boundary, effectively reducing the number of controlling parameters to 5.

The *in vacuo* modes are truncated at $N = 10$ and its sufficiency is demonstrated below by the decaying of modal amplitudes and its comparison with the results of $N = 8$ as well as $N = 20$,

$$\{|A_j|\} = \{1, 6{\cdot}1713, 0{\cdot}4556, 0{\cdot}0240, 0{\cdot}0330, 0{\cdot}0050, 0{\cdot}0090, 0{\cdot}0019\}, \quad N = 8,$$

$$\{|A_j|\} = \{1, 6{\cdot}1892, 0{\cdot}4557, 0{\cdot}0239, 0{\cdot}0330, 0{\cdot}0050, 0{\cdot}0090, 0{\cdot}0019, 0{\cdot}0037, 0{\cdot}0010\}, \quad N = 10,$$

$$\{|A_j|\} = 1, 6{\cdot}1725, 0{\cdot}4556, 0{\cdot}0240, 0{\cdot}0330, 0{\cdot}0050, 0{\cdot}0090, 0{\cdot}0019,$$

$$0{\cdot}0037, 0{\cdot}0010, 0{\cdot}0019, 0{\cdot}0005, 0{\cdot}0011, 0{\cdot}0003, \ldots\}, \quad N = 20.$$

The decaying of $|A_j|$ with respect to j is not strictly monotonous, but the general trend is. Further increase of N does not change the eigenvalue in any significant way, as shown below for the flutter mode given in Figure 3,

$$N = 8 : \omega = 0{\cdot}1292, \quad T = 0{\cdot}1342,$$

$$N = 10 : \omega = 0{\cdot}1294, \quad T = 0{\cdot}1346,$$

$$N = 20 : \omega = 0{\cdot}1292, \quad T = 0{\cdot}1342.$$

We are therefore satisfied with $N = 10$.

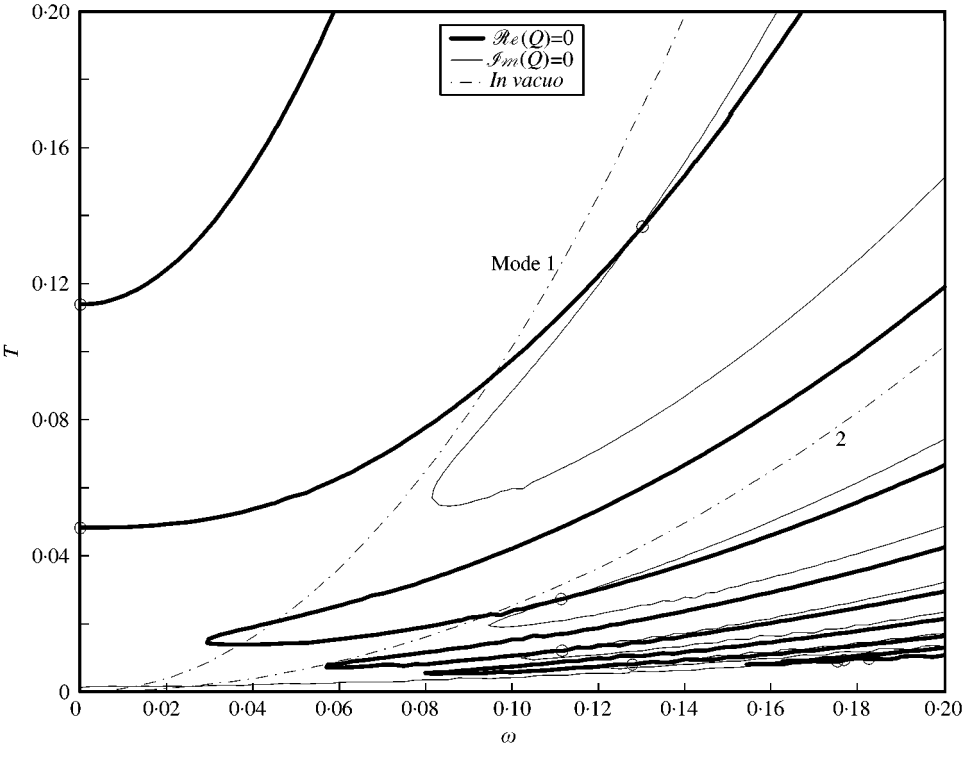

Figure 3. The solution to the eigenequation (10) by the interception of contour curves (—— line for real and —— line for imaginary) for the default parameters chosen in (18). The – · – · – parabolic curves are the *in vacuo* modes (with mode indices marked) shown for reference purpose.

3.1. Basic Example

The process of finding the eigenvalues for the default set of parameters given in equation (18) is shown in Figure 3. The thick and thin lines represent, respectively, the solutions to the real and imaginary parts of the eigenequations in equation (11). The chain-dotted lines, which run through the origin $\omega = T = 0$, are the frictionless, *in vacuo* modes shown here as a reference. The *in vacuo* mode indices are marked along the lines. The frictionless, *in vacuo* modes are found as a parabolic curve by setting $\sigma = 0$ and $P_{jn} = 0$ in equation (9), hence,

$$\boldsymbol{\Pi}_j = 0, \quad \omega_j = \frac{j\pi}{L}\sqrt{\frac{T}{m}}.$$

The open circles in Figure 3 are the eigenmodes found for the fluid-loaded membrane. Two static divergence points are found on the vertical line of $\omega = 0$, and many dynamic instability points are found below the parabolic curve representing the second *in vacuo* mode. The higher value of tension T for the two static divergence points is 0·1123, marginally lower than that of the dynamic instability mode at $\omega = 0{\cdot}1294$, $T = 0{\cdot}1346$. The latter is therefore identified as the critical instability condition in this case. The critical eigenmode is found between the parabolic curves corresponding to the 1st and 2nd *in vacuo* modes. Since the levels of the tensile force required for the static divergence and for the critical dynamic instability are rather close to each other, the two modes may occur together

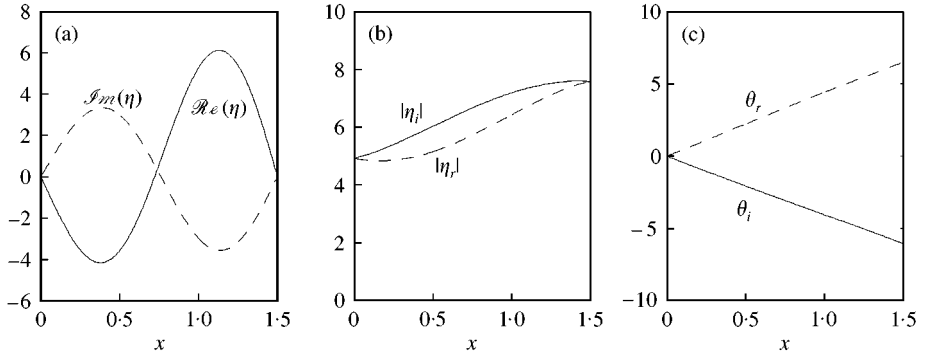

Figure 4. The eigenvibration (flutter) of the membrane at frequency $\omega = 0{\cdot}1294$, and the critical tensile stress $T = 0{\cdot}1346$: (a) displacement $\eta(x)$; (b) amplitude distribution of the decomposed elastic waves, $|\eta_i|$, $|\eta_r|$; (c) phase angle distribution of the decomposed waves.

in practice. In other words, the membrane may collapse and, during the collapse, experience growing oscillations.

The vibration amplitudes at the critical flutter condition are, after normalisation against the first mode,

$$\{A_j\} = \{1,\ -5{\cdot}23 + 3{\cdot}51\mathrm{i},\ 0{\cdot}512 - 0{\cdot}225\mathrm{i},\ 0{\cdot}004 - 0{\cdot}031\mathrm{i}, \cdots\}.$$

The second mode dominates over the first, while the amplitudes of other modes diminish quickly but not monotonously with the mode index, as explained earlier. The real and imaginary parts of the eigenvibration amplitude, $\eta(x)$, are shown in Figure 4(a) by the solid and dashed lines, respectively.

Figure 4(b) shows the amplitudes of the decomposed incident (solid line) and reflected (dashed line) elastic waves [defined in equation (12)]. The incident wave grows along x while the reflected wave decays as it travels upstream. The phase angle distribution is shown in Figure 4(c). Both the incident and the reflected waves have rather constant phase speed, which are, respectively, 87·6%, 80·7% of the *in vacuo* tensile wave speed represented by $\sqrt{T/m}$. When compared with $U^*_{\max}$, the corresponding percentages are, respectively, 3·2 and 3·0%, indicating very slow waves.

The pressure distribution is shown in Figure 5(a). The energy transfer from the fluid to the membrane vibration is calculated by

$$W(x) = \tfrac{1}{2}\,\mathscr{R}e[-p_1(\dot{\eta})^*],$$

where the asterisk outside the brackets denotes the conjugate of a complex number. Note that

$$\int_0^L W(x)\,\mathrm{d}x = W_p + W_\mu.$$

The power distribution $W(x)$ is shown in Figure 5(b). Positive work is done in the upstream part while negative work is done in the downstream part. The total is positive and is balanced out by that consumed by the structural damping. If the membrane vibration is decomposed into incident and reflected elastic waves, the coupling of the total fluid loading with these waves produces power distribution shown in Figure 5(c),

$$W(x) = W_i(x) + W_r(x), \quad W_i(x) = \tfrac{1}{2}\mathscr{R}e\,[-p_1(\dot{\eta}_i)^*], \quad W_r(x) = \tfrac{1}{2}\,\mathscr{R}e[-p_1(\dot{\eta}_r)^*].$$

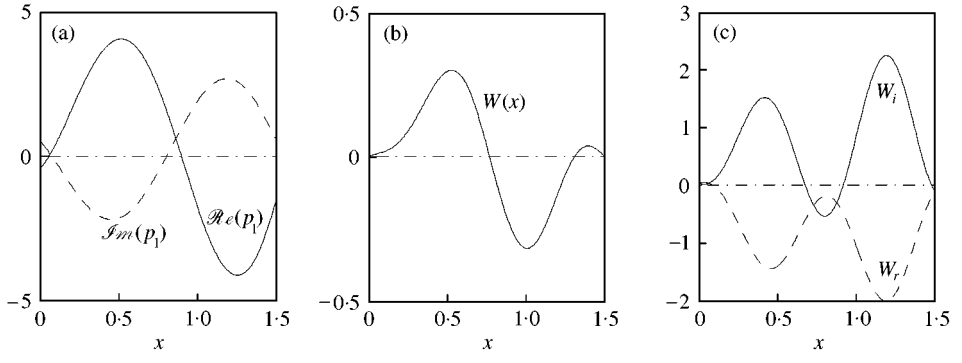

Figure 5. Fluid loading and energy transfer from fluid to the membrane vibration: (a) p_1; (b) flow-to-wall energy flux $W(x)$; and (c) power decomposition into the products of fluid loading with the vibration velocity of the incident (W_i) and reflected (W_r) waves.

The downstream-travelling wave is seen to provide all the energy transfer (solid line) while the reflected wave absorbs most of it (dashed line), leaving a small fraction (about 2%) to be balanced out by the structural damping.

The other way to analyse the fluid–structure coupling is through the modal decomposition. It has been shown in Figure 2(d) that, for the specified first-mode vibration, the fluid loading is against the vibration, namely the work done is negative. In the eigenvibration composed of certain combinations of modes, the work done on the nth modal vibration by the fluid loading caused by the jth modal vibration is calculated as follows:

$$W_{nj} = \tfrac{1}{2}\mathscr{R}e\left\{\int_0^L [-A_j P_{nj}\sin(nx/L)]\,[\mathrm{i}\omega A_n \sin(nx/L)]^*\,\mathrm{d}x\right\} = \frac{\omega L}{4}\mathscr{I}m[-A_j P_{nj}(A_n)^*],$$

while the total work is the sum of all modal combinations, $W = \sum_{n,j} W_{nj}$. The cross-modal fluid-structural coupling is shown below in matrix form for the calculated eigenvibration:

$$W = 10^{-2} \times \sum \overbrace{\begin{matrix} -0{\cdot}9680 & 1{\cdot}1636 & -0{\cdot}1355 & \cdots \\ 7{\cdot}7064 & -4{\cdot}5729 & -1{\cdot}5055 & \cdots \\ -0{\cdot}2141 & 0{\cdot}3154 & -0{\cdot}0700 & \cdots \\ \cdots & \cdots & \cdots & \cdots \end{matrix}}^{\text{Column } j \text{ for modal source of } p_1} \left.\vphantom{\begin{matrix} a \\ a \\ a \\ a \end{matrix}}\right\} \text{Row } n \text{ for } \frac{\partial \eta}{\partial t}.$$

The diagonal elements represent the self-coupling and are all negative, i.e., stable. The main mechanism of energy transfer from the fluid to the membrane comes from W_{21}, namely the coupling between the second-mode vibration velocity and the fluid loading derived from the first-mode vibration. In other words, it is because the fluid loading from the first *in vacuo* mode vibration is not symmetrical about $x = L/2$ as the vibration velocity is, cf. Figure 2(d).

3.2. Effects of Membrane Properties

When the structural loss factor in the basic example increases from $\sigma = 0{\cdot}5$ to 5%, the new pattern of eigenmodes search is shown in Figure 6(a). The marginal dominance of the flutter mode in the original setting (Figure 3) gives way to a clear dominance by static divergence.

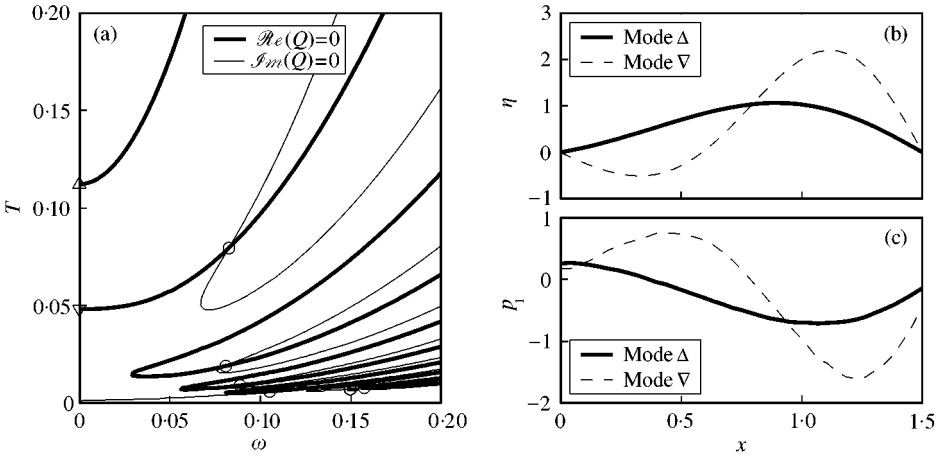

Figure 6. The effect of higher structural damping ($\sigma = 5\%$). The right side up and down triangles plotted on the ordinate in (a) correspond to legends of the two static divergence modes in (b) and (c). (a) The dominance of static divergence at $T = 0{\cdot}1123$ over flutter at $T = 0{\cdot}0796$ and the second static divergence at $T = 0{\cdot}0483$. (b) The eigendistributions of displacement for the two static divergence modes. (c) The fluid loading for the two static divergence modes.

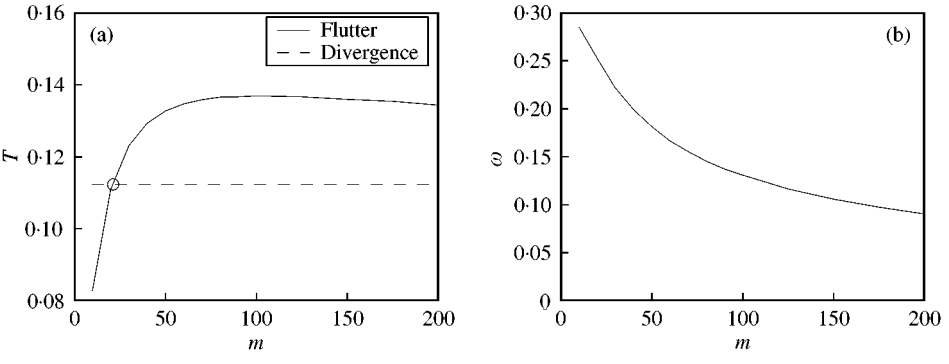

Figure 7. The effect of membrane mass m. (a) The critical tension for static divergence (– – – line) and flutter (—— line). (b) The oscillation frequency of flutter.

The values of T for flutter and divergence are, respectively, 0·0796 and 0·1123, the latter being unchanged from its value at $\sigma = 0{\cdot}5\%$. The dominance of divergence over flutter for higher structural damping is consistent with results of all other theoretical models mentioned in the Introduction. The two static divergence modes are labelled by Δ and ∇, respectively, in Figure 6(a). Their eigendisplacement and pressure distributions are shown in Figure 6(b, c), solid lines being the dominant mode (Δ) and dashed lines the secondary divergence mode (∇). The two modes are dominated by the first and second *in vacuo* modes, respectively. In both modes, the overall effect of the fluid loading is to cause collapse of the membrane, and the tendency of membrane collapse is higher over the downstream portion. Mechanisms leading to the fluid loading asymmetry are explained in Section 2.4.

The effects of the structural inertia are shown in Figure 7. Eigenmodes are separated into two groups corresponding to static divergence and dynamic instabilities, and the mode with the highest value of T in each group is studied. It is found in Figure 7(a) that T for flutter increases with m over most of the range, while that for collapse stays as a constant at 0·1123,

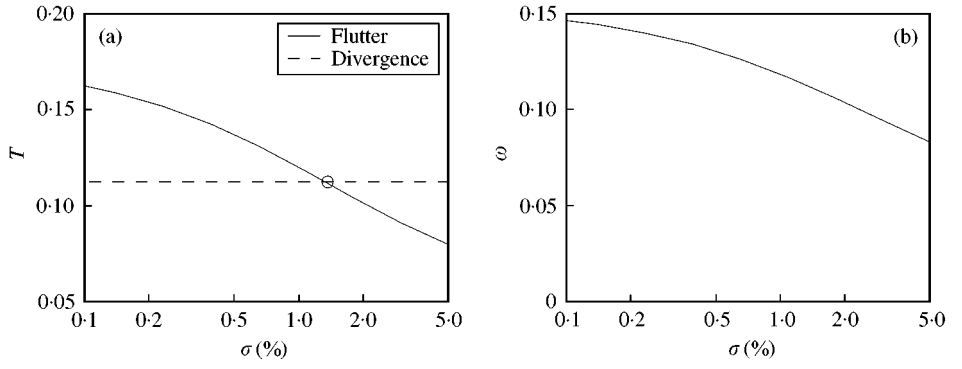

Figure 8. The effect of structural loss factor σ. (a) The critical tension for divergence and flutter as functions of σ. (b) The frequency of flutter oscillation as a function of σ.

the two being equal when $m = 21{\cdot}3$. Below this value, static divergence dominates over flutter, and *vice versa*. This again indicates that the membrane inertia is pro-flutter when it is small. The trend shown in Figure 7(a) also indicates clearly that when $m \to 0$, static divergence is the dominant instability. Figure 7(b) shows the oscillation frequency of the flutter mode as a function of mass ratio. Heavier membranes vibrate at lower frequency.

The effects of the structural loss factor (σ) are shown in Figure (8) using a logarithmic scale, The range chosen for σ is 0·1–5%, but it is pointed out that flutter mode is also found for $\sigma = 0$ at $\omega = 0{\cdot}172$, $T = 0{\cdot}152$, which, if plotted, should be located slightly above that for $\sigma = 0{\cdot}1\%$. A clear distinction between the critical tension levels required for the two types of instability is shown in Figure 8(a). Dominance is reversed at $\sigma = 1{\cdot}4\%$. With lower σ, flutter dominates over divergence, and *vice versa*. Note that the occurrence of static divergence is independent of the structural damping, and a constant level of $T = 0{\cdot}1123$ is shown in Figure 8(a); but the critical tension for flutter does depend on σ. However, the flutter mechanism does not solely depend on energy transfer from the flow to the membrane, since flutter also occurs when $\sigma = 0$. In this case, the surface compliance plays the role of modifying the instability essentially taking place inside the channel flow. Figure 8(b) shows that the flutter frequency decreases with σ, but this is mainly related to the decrease of the critical T shown in Figure 8(a).

Figure 9(a) shows the effect of the membrane length on the critical values of tension for flutter and divergence instabilities, in which all parameters except the length are the default values set in equation (18). Ten calculations are performed for $L = 0{\cdot}5$–$5{\cdot}0$, but Figure 9(a) is zoomed to show only L up to 4 for a better view. Membranes longer than 1·03 experience flutter before divergence, and *vice versa*. This means that longer membranes are unlikely to experience collapse. In fact, membranes longer than about 3 (for this particular case) do not have eigenmodes of static divergence, or have such modes but with very low critical tension. The mode of long-wave static divergence is absent due to the lack of an elastic foundation. This outcome may be appreciated from two perspectives. First, it is easier to excite second and higher *in vacuo* modes on long membranes than on shorter ones, bearing in mind that flutter features the second mode more than the first. Second, downstream-travelling waves tend to grow, while upstream waves decay [see Figures 4(b) and 12(c)]. The net gain of elastic wave energy is used to overcome structural damping. For longer membranes, the downstream-travelling waves have a longer distance in which to grow, but the reflected wave cannot take full advantage of the length, as it decays. The result is that, for the same structural loss factor, longer membranes are more prone to flutter. But it is pointed out that

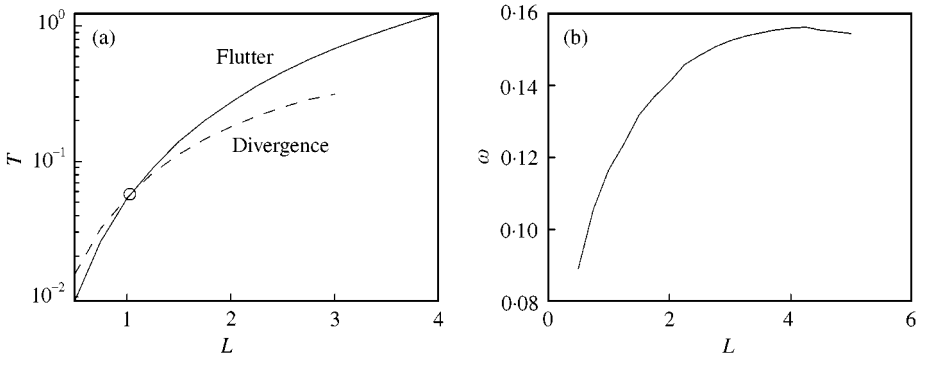

Figure 9. Effect of membrane length. (a) The variation of the critical tension, corresponding to both static divergence and flutter. (b) The oscillation frequency of flutter.

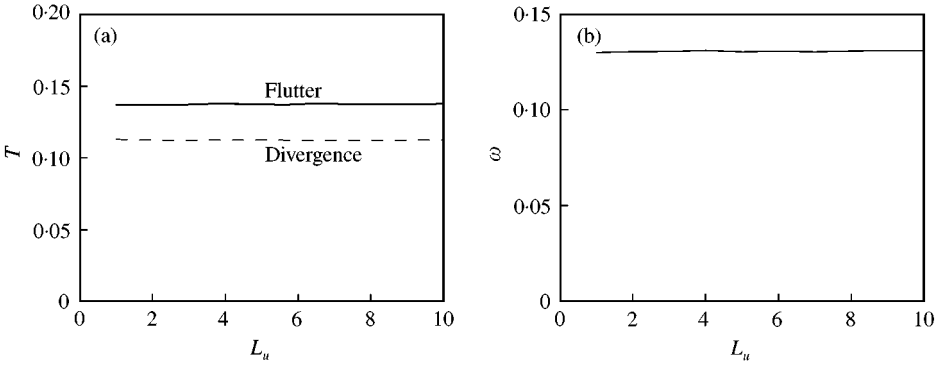

Figure 10. Effect of the upstream distance L_u (a) on the critical tension, and (b) on the flutter frequency.

these conclusions may change when elastic foundations are included in a model which exhibits the 'tube-law' behaviour.

The variation of the flutter frequency is plotted against the membrane length in Figure 9(b). The oscillation frequency increases with the membrane length, an effect accompanied by the increase in the critical tension.

3.3. Effects of Boundary Conditions

There are three factors in the boundary condition: the upstream distance L_u, the downstream distance L_d, and the boundary conditions specified at these two computational borders. The effects of L_u and L_d are studied separately by varying each of these parameters based on the default setting of equation (18) for the blowing type of boundary conditions.

The effects of L_u are shown in Figure 10. There is effectively no influence of L_u on the eigenvalues. This is because all small perturbations die out towards upstream by fluid viscosity, and yet viscosity does not influence the velocity field in the upstream region, since $u = v = 0$ are specified as upstream boundary condition. The pressure on the membrane is only influenced by the downstream distance, since $p' = 0$ is specified at the downstream end.

The effects of downstream distance L_d are shown in Figure 11. It is found in Figure 11(a) that L_d promotes static divergence, which in the present example overtakes flutter when

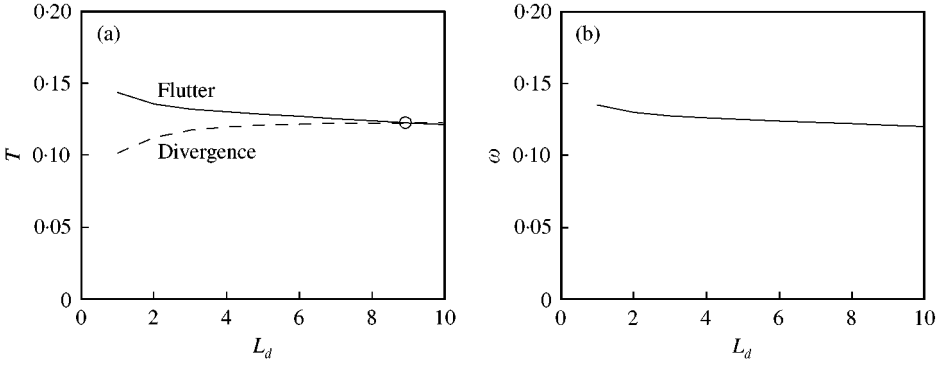

Figure 11. Effect of downstream distance L_d, (a) on the critical tension, and (b) on the flutter frequency.

$L_d = 8{\cdot}9$ (shown as the open circle in the figure). A larger downstream distance decreases the fluid pressure over the membrane as $p' = 0$ is specified downstream. The influence on flutter frequency is not strong, as shown in Figure 11(b).

The current upstream boundary condition fixes the volume flow rate. As a result, there is no velocity perturbation there. At the downstream end, there is no pressure perturbation, which simulates an open end. When the boundary conditions are swapped, upstream and downstream, this then simulates a suction flow with an open upstream entrance (while ignoring the effect of the developing boundary layer). For the suction flow, the perturbation field caused by the *specified* first-mode vibration is shown in Figure 12. The convection of perturbation vorticity above the leeward side of the membrane in Figure 12(a) is similar to that in Figure 2(a). This part of the flow perturbation is mainly related to the membrane displacement. The baseline flow vorticity near the wall is displaced upwards and is carried downstream by the mean flow. The situations for the blowing and suction flows are rather similar, as far as this part of the perturbation flow is concerned. However, the imaginary part of the perturbation flow shown in Figure 12(b) differs from that in Figure 2(b). For suction flow, the downstream part allows no change in the volume flow rate, the displaced fluid is therefore drained through the upstream boundary. The real part of the pressure perturbation shown in Figure 12(c) is similar to that in Figure 2(c). But the imaginary parts differ dramatically in terms of the sign of pressure. In the suction flow, the upstream pressure is fixed, so that the perturbation pressure over most part of the wall is negative, as shown in Figure 12(d). This component of the pressure couples with the vibration velocity and transfers energy from the fluid flow to the membrane.

The character of this coupling may be compared with the argument of negative resistance condition for the Starling-resistor tube oscillation put forward by Conrad (1969, 1995). In that argument, the tube instability is related to the steady flow condition in which increased upstream–downstream pressure drop results in less flow instead of more flow. In our linear analysis with the condition of no change in volume flow rate at the downstream boundary, the steady state is fixed. The same is approximately true for the real part of the perturbation velocity near the inlet boundary, as shown in Figure 12(a). However, the transient flow character displayed by the imaginary part of the velocity perturbation shown in Figure 12 (b) indicates a temporarily reduced flow under the condition of increased pressure drop shown in Figure 12(d). This can be seen as a kind of dynamic negative resistance. Applying a similar analysis for the blowing flow boundary conditions shown in Figure 2, one gets the opposite result. There the specified first mode vibration is stable, and the flutter

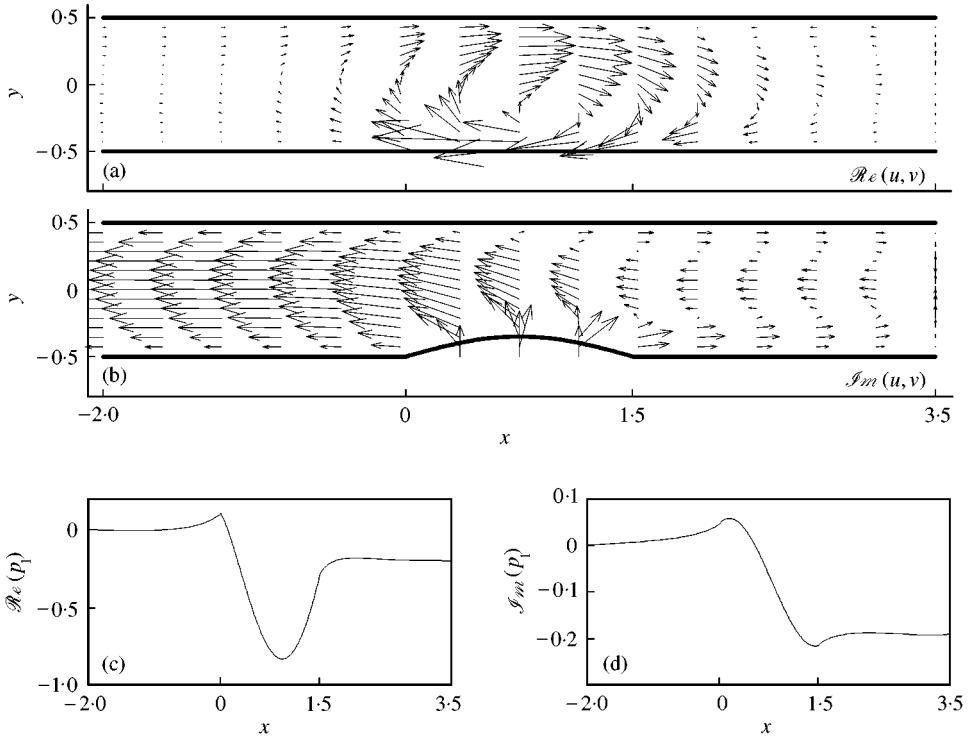

Figure 12. The perturbation flow field and the fluid loading on the wall for the suction flow. All parameters are the same as those in Figure 2. (a) and (b) show, respectively, the real and imaginary parts of $\{u, v\}$, with the wall positions illustrated by the —— lines; (c) and (d) show, respectively, the real and imaginary parts of p_1 on the wall.

is actually caused by the cross-modal coupling, which is absent in the studies of Conrad (1969) and most other experiments of this kind.

The eigenvibration modes for the suction flow are shown in Figure 13. The contour-crossing shown in Figure 13(a) indicates the dominance of the flutter mode (indicated by an open circle) at ($\omega = 0{\cdot}9332$, $T = 20{\cdot}79$) over the divergence mode which is too low to be seen in the figure and will not be analysed further. This contrasts sharply with the flutter predicted for the blowing-type boundary conditions at ($\omega = 0{\cdot}1294$, $T = 0{\cdot}1346$) in Figure 3. The oscillation frequency is much higher, and the critical tension is also much higher. For a given membrane tension, the higher value of T means a much lower value of flow velocity when flutter occurs. In other words, the suction flow is much more prone to flutter than the blowing flow. The eigenfrequency is found to be slightly below that of the first *in vacuo* mode ($\omega_1 = 0{\cdot}9632$), in contrast with the case of blowing flow. The eigendisplacement shown in Figure 13(c) is also quite different from its counterpart in Figure 4(a). Here the first mode dominates and there is little second or higher-order modes. The pressure distribution is shown in Figure 13(d). Note that in Figure 13(c) and 13(d), the imaginary parts (dashed lines) are magnified by 50 and 5 times, respectively, so that they can be seen clearly. Comparing the distribution of the displacement (η) in Figure 13(c), with the distribution of the fluid loading (p_1) in Figure 13(d), it is found that they have roughly an antiphase relationship, for both real and imaginary parts. In other words, the fluid loading tends to collapse the membrane further. The fluid-wall energy transfer, $W(x)$, is shown in Figure

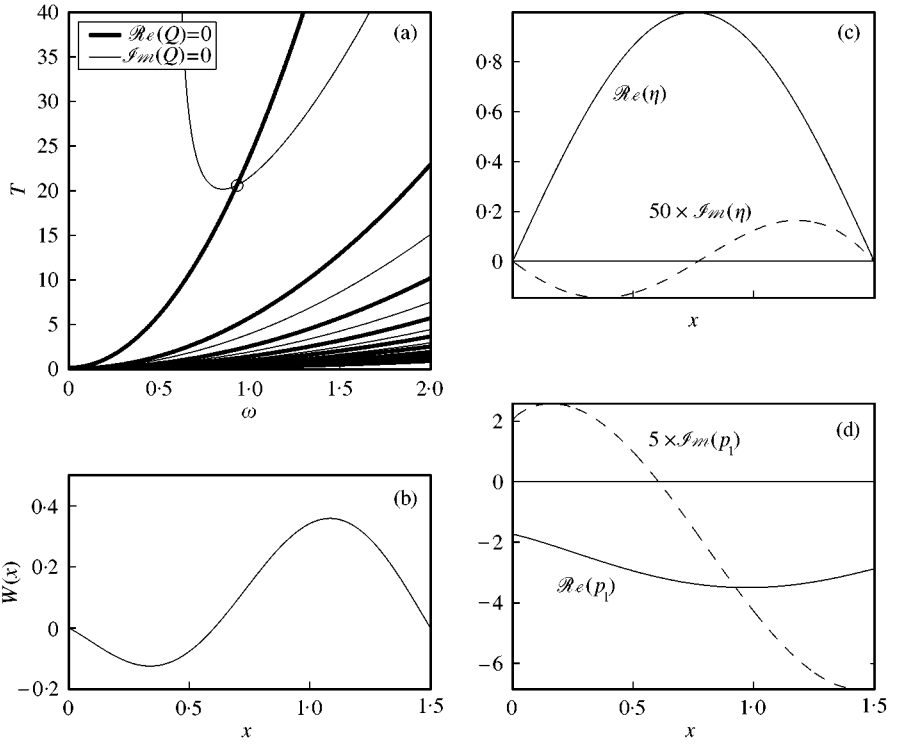

Figure 13. The solution for the suction flow boundary conditions. All parameters are the same as those of equation (18) except the inlet and exit boundary conditions. (a) The solution for the eigenequation (10) by the contour-crossing method. (b) The work done by the fluid on the membrane, (c) The eigendisplacement η. (d) The fluid loading distribution p_1. In (c) and (d), the imaginary parts are magnified by a factor of 50 and 5, respectively, for clarity.

13(b). The pattern of $W > 0$ in the downstream part and $W < 0$ in the upstream part is exactly opposite to the pattern shown for the blowing flow in Figure 5(b). In terms of cross-modal coupling, the flow-to-membrane energy transfer is given by

$$W = 10^{-2} \times \sum \overbrace{\begin{matrix} -15{\cdot}2779 & 0{\cdot}0594 & -0{\cdot}0179 & \cdots \\ 0{\cdot}0003 & -0{\cdot}0001 & -0{\cdot}0000 & \cdots \\ -0{\cdot}0000 & 0{\cdot}0001 & -0{\cdot}0000 & \cdots \\ \cdots & \cdots & \cdots & \cdots \end{matrix}}^{\text{Column } j \text{ for modal source of } p_1} \left.\begin{matrix} \\ \\ \\ \\ \end{matrix}\right\} \text{Row } n \text{ for } \frac{\partial \eta}{\partial t}.$$

The energy transfer mainly derives from the self-coupling of the first mode. In terms of the membrane vibration velocity, decomposed into the incident and reflection waves, the coupling between the fluid loading with the incident wave is unstable while that with the reflected wave is stable, similarly to what is found for the blowing flow in Figure 5(c).

Since the flutter mode is predominantly the first *in vacuo* mode ($|A_1/A_2| = 280{\cdot}3$ for the above example), we may take a one-mode approximation ($N = 1$) to examine the dynamics of the membrane vibration. Equation (9) is simplified and split into real and imaginary

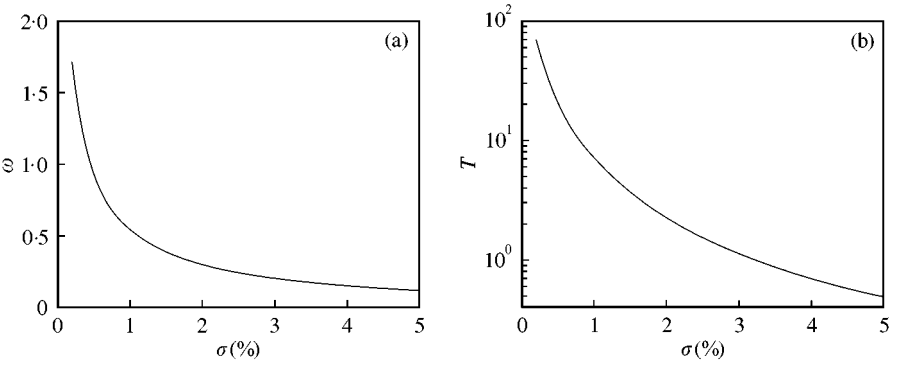

Figure 14. Variation of (a) flutter frequency and (b) critical tension as functions of structural damping.

TABLE 2
Results of energy conservation analysis for the default eigenflutter mode

Source term	Result	Outgoing flux	Result
Viscous source	$S_J = 16{\cdot}3510$	To upstream	$F_u = 0$
Bulk dissipation	$S_\Psi = 14{\cdot}3299$	To downstream	$F_d = 0{\cdot}01343$
Vortical absorption	$S_\Theta = 1{\cdot}9171$	To membrane	$F_m = 0{\cdot}03225$
Net source	0·1041	Total flux	0·0457

parts, which can be solved for eigenvibration frequency and critical tension, i.e.,

$$\Pi_1 + P_{11} \approx 0, \quad \text{where } \Pi_1 = m\omega^2(-1 + \mathrm{i}\sigma) + T(\pi/L)^2.$$

$$\text{Real: } -m\omega^2 + T(\pi/L)^2 + \mathscr{R}e(P_{11}) \approx 0, \quad \text{Imaginary: } m\omega^2\sigma + \mathscr{I}m(P_{11}) \approx 0.$$

$$\text{Solution: } \omega \approx \sqrt{-\mathscr{I}m(P_{11})/(m\sigma)}, \quad T \approx -[\mathscr{R}e(P_{11}) + \mathscr{I}m(P_{11})/\sigma](L/\pi)^2.$$

Here P_{11} is the first mode coefficient of the fluid loading caused by the first mode vibration. For the eigenvibration frequency shown in Figure 5, $P_{11} = -3{\cdot}9864 - 0{\cdot}4366\mathrm{i}$. The critical tension estimated by the above approximate solution is 20·82, which is very close to the 10-mode result of $T = 20{\cdot}79$. Of course, P_{11} is a function of ω and the above solution is strictly speaking an implicit one. It would be interesting to examine the variation of the eigenvibration frequency as a function of σ for the 10-mode modelling. The results are shown in Figure 14(a), which confirms the trend of $\omega \propto \sigma^{-1/2}$. This means that $\mathscr{I}m(P_{11}) < 0$ is the essential feature responsible for flutter in suction flow, and that mode 1 self-coupling is the origin of energy transfer.

3.4. Effect of Viscosity

In Section 2.4, viscosity has been shown to play a pivotal role in creating perturbation energy during a specified motion of the membrane. The eigenflutter mode has been predicted at $\omega = 0{\cdot}1294$, $T = 0{\cdot}1346$ for the default set of parameters shown in equation (18). We now analyse the energy balance for the flutter eigenmode. The error for the energy conservation

$$S_J - S_\Psi - S_\Theta = F_u + F_d + F_m,$$

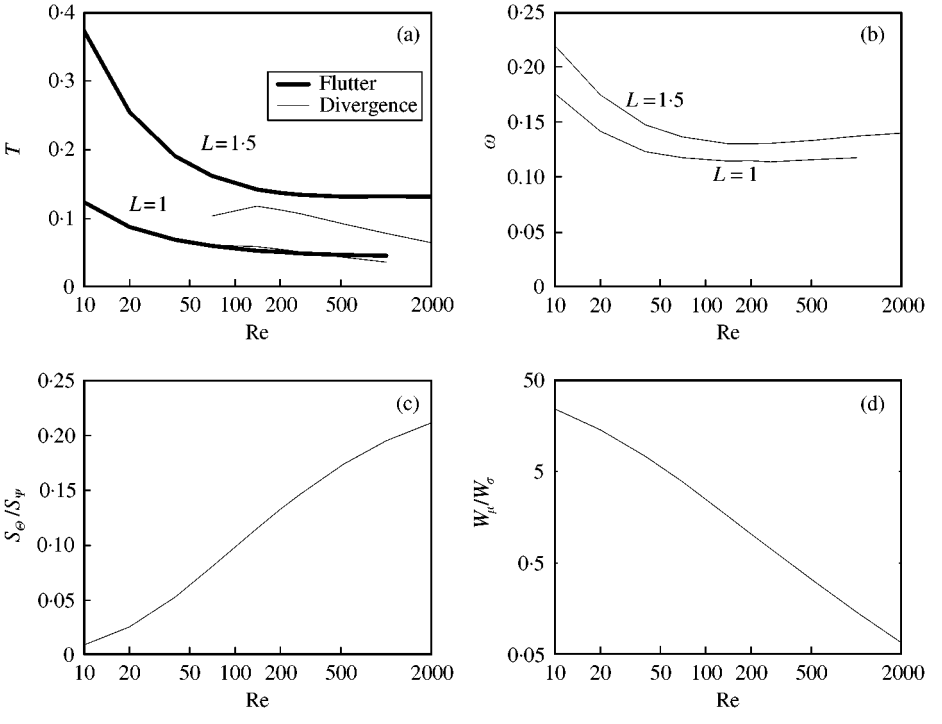

Figure 15. Fluid viscosity effects. (a) Critical tension for flutter (—— lines) and static divergence (—— lines) for two membrane lengths, $L = 1{\cdot}5$ and $1{\cdot}0$; (b) the flutter frequency for the two membranes; (c) the vortical absorption of fluctuation energy S_Θ normalised by the viscous dissipation S_Ψ; (d) ratio of fluid viscous stress work done on the membrane W_μ relative to the structural damping of the membrane W_σ.

amounts to 0·0584. This is very small compared with, say, S_Θ, the ratio being 3%, and is even more insignificant when compared with the largest component in the energy conservation equation, S_J. This comparison serves as a measure of how accurate the numerical tool is. Note that the error is partly contributed to by the streamwise diffusion technique whose error vanishes as the mesh size decreases. Although this error is comparable to the energy transferred to the wall, F_m, one should assess the accuracy in this aspect by examining the energy balance of the membrane vibration as written in equation (15). The balance for the calculated flutter mode is

$$\underset{0{\cdot}01588}{W_\sigma} = \underset{0{\cdot}03225}{W_p} + \underset{-0{\cdot}01674}{W_\mu},$$

the numerical error being 2·3% relative to W_σ. The fact that the energy terms such as S_J and W_p differ by many orders of magnitude does not mean very weak fluid-structural coupling. But rather, it derives from the fact the structural loss factor is specified to be a very small quantity, which in this case is $\sigma = 0{\cdot}5\%$. Despite the difference in magnitude, the role played by fluid viscosity is definitely one of destabilisation, and the role played by the structural damping is one of stabilisation, as shown in Figure 8. The former statement is further confirmed by the variation of critical tension with respect to the fluid viscosity μ, as shown in Figure 15. It can be seen from Figure 15(a), which also includes the results for a shorter membrane $L = 1$, that the critical tension increases as viscosity increases towards lower Reynolds number (Re). When Re is very high, the critical tension settles down to a rather

constant value. But the same is not true for static divergence. For the default length of $L = 1{\cdot}5$, the critical tension for flutter is always higher than that of static divergence. For $L = 1$, the eigentension for flutter and divergence coincides at two viscosity values. The influence of Reynolds number on frequency is more subtle, as shown in Figure 15(b). Figure 15(c) shows the vortical absorption of fluctuation energy (S_Θ) normalised by the viscous dissipation (S_Ψ), and Figure 15(d) shows the ratio of work done by the viscous stress on membrane (W_μ) to the power consumed by the structural internal friction (W_σ). Both figures indicate that the effect of fluid viscosity decreases as Reynolds number increases, which is consistent with normal expectation. The stabilisation role played by fluid viscosity through W_μ competes with the destabilisation effect through S_J, which together give a minima in the functional relationship between T and Re. The minima can be found on the thick solid lines in Figure 15(a), but their locations are obscured by the rather flat portion of the curve in the region of high Reynolds numbers. For $L = 1{\cdot}5$, the lowest value of T is 0·1310 and it occurs at $\mathrm{Re} = 624$.

4. CONCLUDING REMARKS

As explained earlier, a laboratory model comparable to the current theoretical model is yet to be constructed. The current analysis is based on the parallel flow model and is unlikely to compare well quantitatively with experiments in which the flow pattern is highly three-dimensional and the oscillations are highly nonlinear. The critical flow velocity at which flutter occurs in a parallel flow channel is likely to be much higher than that needed for a collapsed tube flow. In other words, T predicted in our analysis may seem to be rather low when compared with that found in a Starling-resistor experiment. Nevertheless, the following conclusions can be drawn.

1. Flutter and divergence may occur at similar flow velocities, and may coexist. Flutter and divergence exchange dominance when the wall properties change. Membrane inertia and membrane length are pro-flutter, while structural damping suppresses oscillation resulting in divergence as the main instability mode.

2. Conditions at the upstream and downstream ends of the channel have crucial effects on the characteristics of the membrane instability. Two conditions are simulated in the present study. One is called the blowing flow in which the upstream part has a fixed volume flow rate while the downstream one has a fixed pressure. The other is called the suction flow in which the upstream part has a fixed pressure while the downstream one has a fixed volume flow rate. For blowing flow, the upstream distance does not have a significant effect on the results when $u = v = 0$ is specified at the upstream boundary, but the downstream distance is found to decrease the threshold for static divergence. For the blowing flow, the coupling of the fluid loading induced by the first *in vacuo* mode vibration and the vibration velocity of the second *in vacuo* mode dominates the flutter mechanism. For the suction flow, the self-coupling of the first *in vacuo* mode is unstable and dominates the activities of other modes. A dynamic version of Conrad's negative resistance argument is put forward to elucidate the instability mechanism in suction flow.

3. The elastic waves over a finite membrane have a standing wave pattern which can be decomposed into up- and downstream-travelling waves. The component of the downstream-travelling wave is responsible for energy transfer from the fluid to the wall. The prevalence of flutter increases with membrane length, while that of static divergence decreases. The findings in this particular aspect are therefore consistent with our earlier theory (Huang 1998) regarding the instability of slow elastic waves exposed to shear flows. However, when the effects of the reflection waves are accounted for, the total work done by

the shear-flow terms, S_Θ, is negative, contrasting with the destablisation role projected for S_Θ in the case of a single downstream-travelling wave. The finding that a longer membrane is more prone to flutter than static divergence can be appreciated from the observation that there is more chance for downstream-travelling waves to gain energy from the flow and grow on a longer membrane.

4. For very short membranes, for which the traditional tube-law is least satisfactory, it is perhaps more appropriate to appreciate the results from the perspective of cross-modal coupling. Flutter is found to arise from the coupling of the second-mode vibration velocity and the fluid loading caused by the first-mode vibration. The emergence of the second and higher-order modes can be analysed as follows. When a shear flow passage is narrowed by the membrane, excess vorticity near the wall is displaced and the convection of perturbation vorticity form a pattern of perturbation "vortex" at the leeward side of a displaced membrane [Figures 2(a) and 12(a)]. This perturbation "vortex" gives a particular portion of the wall membrane more suction force than elsewhere, creating an asymmetric fluid loading. The asymmetric loading promotes oscillation of the second and higher-order *in vacuo* modes. The features of the flutter instabilities also depend crucially on the upstream and downstream boundary conditions. For suction flows, the flutter mode is almost entirely in the form of the first *in vacuo* mode.

5. The role played by the fluid viscosity is destabilising, similar to that in Tollmien–Schlichting waves. In our energy conservation analysis, viscous terms are split into surface source terms and bulk dissipation terms. It is shown that the former always dominate over the latter and yield net viscous source of fluctuation energy. The perturbation of mean flow vorticity also creates a source term which is found to be negative. In other words, it is a term of vortical absorption of fluctuation energy. The vortical absorption takes most of the energy created by the viscous terms, leaving a small fraction to drive the membrane vibration. The energy imparted to the membrane vibration through the action of the normal pressure overcomes both the normal viscous stress ($2\mu\partial v/\partial y$) and the membrane structural friction. The destabilising role played by fluid viscosity is confirmed by the variation of critical membrane tension with respect to fluid viscosity when the Reynolds number is moderate; but at higher Reynolds numbers, the stabilising effect of the normal viscous stress begins to dominate, creating a most unstable Reynolds number for a given set of geometric configurations.

References

Berry, B. S. 1992 Damping mechanisms in thin-layer materials. In *M^3D: Mechanics and Mechanisms of Material Damping* (eds V. K. Kinra & A. Wolfenden), ASTM STP 1169, pp. 28–44. Philadelphia: American Society for Testing and Materials.

Bertram, C. D. & Castles, R. J. 1999 Flow limitation in uniform thick-walled collapsible tubes. *Journal of Fluids and Structures* **13,** 399–418.

Bertram, C. D. & Godbole, S. A. 1997 LDA measurements of velocities in a simulated collapsed tube. *ASME Journal of Biomechanical Engineering* **119,** 357–363.

Bertram, C. D., Raymond, C. J. & Pedley, T. J. 1990 Mapping of instabilities for flow through collapsed tubes of different length. *Journal of Fluids and Structures* **4,** 125–153.

Cancelli, C. & Pedley, T. J. 1985 A separated-flow model for collapsible-tube oscillations. *Journal of Fluid Mechanics* **157,** 375–404.

Caro, C. G., Pedley, T. J., Schroter, R. C. & Seed, W. A. 1978 *The Mechanics of the Circulation.* Oxford: Oxford University Press.

Carpenter, P. W. & Garrad, A. D. 1986 The hydrodynamic stability of flow over Kramer-type compliant surfaces. Part 2. Flow-induced surface instabilities. *Journal of Fluid Mechanics* **170,** 199–232.

Conrad, W. A. 1969 Pressure-flow relationships in collapsible tubes. *IEEE Journal of Biomedical Engineering* **16,** 284–295.

CONRAD, W. A. 1995 Relationship of pressure wave velocity to self-excited oscillation of collapsible-tube flow — discussion. *JSME International Journal*, Series A **38,** 138.

DAVIES, C. & CARPENTER, P. W. 1997*a* Numerical simulation of the evolution of Tollmien–Schlichting waves over finite compliant membranes. *Journal of Fluid Mechanics* **335,** 361–392.

DAVIES, C. & CARPENTER, P. W. 1997*b* Instabilities in a plane channel flow between compliant walls. *Journal of Fluid Mechanics* **352,** 205–243.

FUNG, Y. C. 1993 *Biomechanics*: *Mechanical Properties of Living Tissues*. New York: Springer-Verlag.

GAVRIELY, N., SHEE, T. R., CUGELL, D. W. & GROTBERG, J. B. 1989 Flutter in flow-limited collapsible tubes: a mechanism for generation of wheezes. *Journal of Applied Physiology* **66,** 2251–2261.

GROTBERG, J. B. 1994 Pulmonary flow and transport phenomena. *Annual Review of Fluid Mechanics* **26,** 529–571.

GROTBERG, J. B. & REISS, E. L. 1984 Subsonic flapping flutter. *Journal of Sound and Vibration* **92,** 349–361.

GROTBERG, J. B. & SHEE, T. R. 1985 Compressible-flow channel flutter. *Journal of Fluid Mechanics* **159,** 175–193.

HUANG, L. 1998 Reversal of the Bernoulli effect and channel flutter. *Journal of Fluids and Structures* **12,** 131–151.

HUANG, L., QUINN, S. J., ELLIS, P. D. M. & FFOWCS WILLIAMS, J. E. 1995 Biomechanics of snoring. *Endeavour* **19,** 96–100.

JENSEN, O. E. 1990 Instabilities of flow in a collapsed tube. *Journal of Fluid Mechanics* **220,** 623–659.

KAMM, R. D. & PEDLEY, T. J. 1989 Flow in collapsible tubes: a brief review. *ASME Journal of Biomechanical Engineering* **111,** 177–179.

KECECIOGLU, I., MCCLURKEN, M. E., KAMM, R. D. & SHAPIRO, A. H. 1981 Steady, supercritical flow in collapsible tubes. Part 1. Experimental observations. *Journal of Fluid Mechanics* **109,** 367–389.

KUMARAN, V. 1995*a* Stability of the viscous flow of a fluid through a flexible tube. *Journal of Fluid Mechanics* **294,** 259–281.

KUMARAN, V. 1995*b* Stability of the viscous flow of a fluid through a flexible tube at high Reynolds number. *Journal of Fluid Mechanics* **302,** 117–139.

LAROSE, P. G. & GROTBERG, J. B. 1997 Flutter and long-wave instabilities in compliant channels conveying developing flows. *Journal of Fluid Mechanics* **331,** 37–58.

LIGHTHILL, M. J. 1962 Physical interpretation of the mathematical theory of wave generation by wind. *Journal of Fluid Mechanics* **14,** 385–398.

LUO, X. Y. & PEDLEY, T. J. 1996 A numerical simulation of unsteady flow in a two-dimensional collapsible channel. *Journal of Fluid Mechanics* **314,** 191–225.

LUO, X. Y. & PEDLEY, T. J. 1998 The effects of wall inertia on flow in a two-dimensional collapsible channel. *Journal of Fluid Mechanics* **363,** 253–280.

MATSUZAKI, Y. & FUNG, Y. C. 1977 Stability analysis of straight and buckled two-dimensional channels conveying an incompressible flow. *Journal of Applied Mechanics* **44,** 548–552.

MATSUZAKI, Y. & FUNG, Y. C. 1979 Non-linear stability analysis of a two-dimensional model of an elastic tube conveying a compressible flow. *Journal of Applied Mechanics* **46,** 31–36.

MILES, J. W. 1957 On the generation of surface waves by shear flows. *Journal of Fluid Mechanics* **3,** 185–204.

MÖHRING, W. 1971 Energy flux in duct flow. *Journal of Sound and Vibration* **18,** 101–109.

MORFEY, C. L. 1971 Acoustic energy in non-uniform flows. *Journal of Sound and Vibration* **14,** 159–170.

PEDLEY, T. J. & STEPHANOFF, K. D. 1985 Flow along a channel with a time-dependent indentation in one wall: the generation of vorticity waves. *Journal of Fluid Mechanics* **160,** 337–367.

PEDRIZZETTI, G. 1998 Fluid flow in a tube with an elastic membrane insertion. *Journal of Fluid Mechanics* **375,** 39–64.

SHAPIRO, A. H. 1977 Steady flow in collapsible tubes. *ASME Journal of Biomechanical Engineering* **99,** 126–147.

TANG, D. L., YANG, C. & KU, D. N. 1999 A 3-D thin-wall model with fluid–structure interactions for blood flow in carotid arteries with symmetric and asymmetric stenoses. *Computers and Structures* **72,** 357–377.

WEAVER, D. S. & PAÏDOUSSIS, M. P. 1977 On collapse and flutter phenomena in thin tubes conveying fluid. *Journal of Sound and Vibration* **50,** 117–132.